Deriving Nebular Dust Attenuation Curves based on Simulated Galaxies

High energy & Optical/Infrared Astrophysics,
Department of Physics, Faculty of Science, Hiroshima University

B193396
Mau Otsuki

February 22, 2024

指導教員　Yasushi Fukazawa
　　主査　Hanae Inami
　　副査　Masao Kuriki

Abstract

Dust in galaxies attenuates light by absorption and scattering. Without correcting for dust attenuation, the true characteristics of galaxies elude us. To address this issue, an attenuation curve, which describes the amount of attenuation as a function of wavelength, is typically used for the correction. However, attenuation curves are known to vary from galaxy to galaxy, and their relations to galaxy properties are still under debate. In this work, I take an approach of deriving dust attenuation curves by comparing hydrogen recombination line ratios of simulated galaxies with their theoretically estimated values. I focus on 10 of these lines in the spectral range from 0.41 μm (Hδ) to 4.05 μm (Brα) to calculate attenuations for each line, then fit them with several forms of functions to create the curves. By using the spectra of 100 simulated galaxies, I derive each of their attenuation curves and investigate whether there are any correlations between the attenuation curves and galaxy properties.

Contents

List of Figures

List of Tables

Chapter 1

Introduction

1.1 Dust in galaxies

1.1.1 Dust in galaxy evolution

Galaxies encompass stars, gas, dark matter, and dust. Dust consists of microscopic solid particles made of elements such as C, Si, O, Mg, Fe, with sizes typically ranging from 0.01 to 1 μm. Coexisting with gas, dust is estimated to constitute approximately 1% of the mass of the interstellar medium (ISM) in galaxies (Fukui et al. 2008; Taniguchi et al. 2018). Despite representing a smaller fraction of mass compared to the other components in galaxies, such as gas and star, an understanding of dust is imperative for comprehending galaxies. For example, dust plays an important role in the formation of parent clouds of stars: molecular clouds. Hydrogen atoms alone cannot form H_2 molecules but need a dust surface as a catalyst (Fukui et al. 2008). Dust also absorbs ultraviolet (UV) photons from outside of the molecular clouds shielding molecules from photodissociation (Fukui et al. 2008). Additionally, dust aids the cooling of star-forming clouds by shielding them from UV light which provokes photoelectric heating in ISM (Klessen and Glover 2016). Cooling is vital for gas clouds to collapse and form stars. Gravitational collapse raises pressure and hampers any further collapse. Whether or not a cloud will further collapse depends on the balance between the cooling and the temperature rise caused by the compression (Umemura et al. 2016). In other words, the drop in temperature of the cloud, together with the conversion of the particles from atomic to molecular, decreases the Jeans mass, above which the cloud will collapse by its own gravitation (Klessen and Glover 2016; Karttunen et al. 2007). On the other hand, dust is also thought to work in limiting star formation in massive star clusters. With its high opacity, dust is more susceptible to radiation pressure from the light of stars (Mac Low 2013; Umemura et al. 2016). As these examples show, dust is indispensable when talking about galaxy formation and evolution.

1.1.2 Dust extinction and attenuation

In addition to the roles of dust in galaxies mentioned above, dust significantly alters how we see galaxies because it reprocesses the light while travelling to us. Since dust attenuates (absorbs and scatters) light, especially in shorter wavelengths like UV and optical, and reemits the energy in the infrared (IR) (Fukui et al. 2008), we must take these effects into consideration when analysing observational data of galaxies.

Consider a situation where we observe an object at wavelength λ. If the intrinsic (attenuation-free) apparent magnitude is $m_{\lambda 0}$ and the attenuation that the object suffers is A_λ, the observed (attenuated)
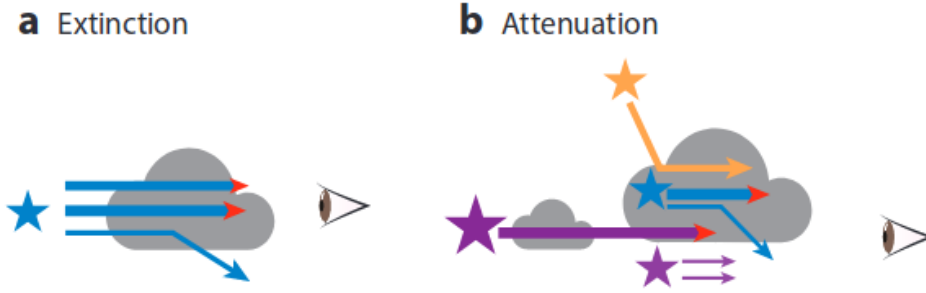
Figure 1.1. Comparison of extinction and attenuation: (a) for extinction and (b) for attenuation. This figure is taken from Salim and Narayanan (2020)

apparent magnitude m_λ is given by:

$$m_\lambda = m_{\lambda 0} + A_\lambda \tag{1.1}$$

in magnitudes (Salim and Narayanan 2020). Here, A_λ is the apparent magnitude of attenuation, and thus it can be interpreted in two different ways depending on the observed object; it is referred to as 'extinction' when the object is more like a point source, and for an extended object like a galaxy, it is referred to as 'attenuation'. The difference is schematically shown in Figure 1.1. Hereafter, I regard A_λ as attenuation in this thesis, irrespective of object types.

This variation is attributed to the types of processes considered. Extinction is only for a specific line of sight. It only represents the amount of light lost by absorption and scattering along the line of sight and does not account for light from other directions. Thus, extinction is not sufficient for dealing with extended objects. Attenuation, on the other hand, is the net loss of light from multiple lines of sight. It includes not only the light loss due to absorption and scattering, but also the light gained by scattering and other geometric effects. As depicted by the purple stars in Fig 1.1 (b), some of the light suffers more/less attenuation because of the geometry.

Another commonly used method for explaining attenuation is optical depth (or optical thickness) τ_λ. Here, I will clarify the relationship between optical depth and extinction/attenuation to avoid any confusion. Optical depth is expressed in

$$I_\lambda = I_{\lambda 0} e^{-\tau_\lambda} + \int_0^{\tau_\lambda} e^{-(\tau_\lambda - \tau'_\lambda)} S_\lambda(\tau'_\lambda) d\tau'_\lambda, \tag{1.2}$$

where $I_{\lambda 0}$ is the unattenuated intensity, I_λ is the observed (and hence attenuated) intensity, and $S_\lambda(\tau'_\lambda)$ is the source function, which represents the increase of light due to scattering and emission at τ'_λ from the observer (Umemura et al. 2016). The first term on the right-hand side quantifies how much light from the object is absorbed and scattered away along the line of sight, whereas the second term describes newly entered light somewhere between the object and the observer due to emission or scattering. Although Equation (1.2) includes an increase of light due to scattering, it does not correspond to 'attenuation' because we only consider a single sightline in this equation. To compare with 'extinction', let us ignore the second term. Since the distance for $I_{\lambda 0}$ and I_λ is the same here, we can convert Equation (1.2) to

apparent magnitudes by using the definition of apparent magnitude:

$$-2.5\log_{10}I_\lambda = -2.5\log_{10}I_{\lambda 0} + 2.5\frac{\tau_\lambda}{\log_e 10} \tag{1.3}$$

$$m_\lambda = m_{\lambda 0} + 2.5\frac{\tau_\lambda}{\log_e 10}. \tag{1.4}$$

Comparing Equation (1.4) to Equation (1.1), we obtain

$$A_\lambda \simeq 1.0857\tau_\lambda. \tag{1.5}$$

Thus, 'extinction' is comparable to optical depth (which is practically proportional to column density) if we exclude light increasing effects due to emission and scattering. In contrast, optical depth alone cannot provide a comprehensive explanation for 'attenuation', still embracing some link to it.

1.2 Dust attenuation curves of galaxies

1.2.1 Variety of attenuation curves

In this section, reference is frequently made to the review Salim and Narayanan (2020) and references therein.

Characterisation of curves

First, I will discuss various shapes of extinction/attenuation curves. When we refer to the shape of a curve, it is about the curve that has undergone a normalisation. The normalisation methods varies in different studies, but A_V (attenuation A_λ at V band corresponding to ~0.55 μm) and $E(B-V) = A_B - A_V$ (reddening, the difference of attenuation at B band (~0.44 μm) and V band) are commonly used. In this subsection, curves are normalised by A_V, denoted as A_λ/A_V.

To make comparisons of curves easier, I employ several forms of slopes to boil them down as shown in Figure 1.2:
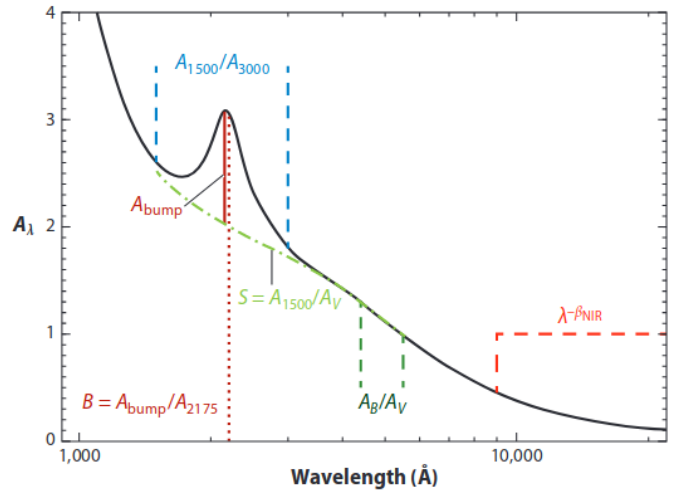

Figure 1.2. The average Milky Way extinction curve (black line). Illustrated with colors are the slopes (Equation (1.6)–(1.9)) and the 2175 Å bump (Equation (1.10)). The figure is taken from Salim and Narayanan (2020)
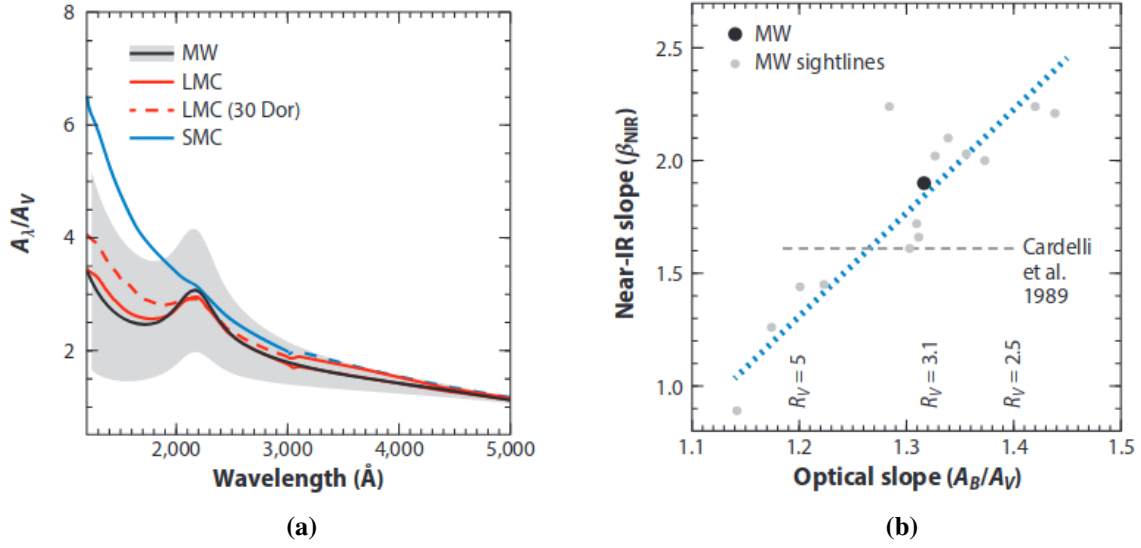
Figure 1.3. (a) Extinction curves of the MW sightlines (black for the average and grey for different sightlines), the LMC (red), and the SMC (blue). (b) The NIR slope versus the optical slope of the MW sightlines (grey points) and the average MW (black). The blue dotted line is the inferred relationship (Equation (1.11)) on which the MW sightlines obey. The horizontal grey dashed line represents the constant value presented in a past study. The figure is taken from Salim and Narayanan (2020)

$$A_{1500\text{Å}}/A_{3000\text{Å}} \quad \text{(UV slope)}, \tag{1.6}$$

$$A_B/A_V \quad \text{(optical slope)}, \tag{1.7}$$

$$A_{1500\text{Å}}/A_V \quad \text{(UV-optical slope)}, \tag{1.8}$$

$$\text{and} \quad A_\lambda/A_V = (\lambda/5500\text{Å})^{-\beta_{\text{NIR}}} \quad \text{(NIR slope, } \beta_{\text{NIR}}). \tag{1.9}$$

The near-infrared (NIR) slope covers the range between 0.9 μm and 2–5 μm. In addition, we can use arbitrary combinations of attenuation to represent the curves. The extinction curve of the average Milky Way (MW) exhibits a bump feature at ~2175 Å (see Figure 1.2). The following parameter quantifies its relative strength to the baseline attenuation at 2175 Å:

$$A_{\text{bump}}/A_{2175\text{Å}}. \tag{1.10}$$

Variety of 'extinction' curves

Here, I introduce some consensus regarding the variety of 'extinction' curves derived from observations of different MW sightlines and the Large/Small Magellanic Clouds (LMC/SM):

1. Across all the MW, the LMC, and the SMC sightlines, the extinction curve becomes shallower (or greyer) as A_V increases (optically thicker).

2. Both the MW and the LMC exhibit the 2175 Å bump feature. A star-forming region in the LMC (30 Dor) displays a weaker bump, while the SMC shows virtually no bump (Figure 1.3a).

3. The strength of 2175 Å bump increases when the optical slope is steeper in the MW sightlines. This is not true for the SMC and the LMC's star-forming region.

7

4. A relationship is found between the NIR slopes and the optical slopes of the MW sightlines (Figure 1.3b):

$$\beta_{\mathrm{NIR}} = 4.59(A_B/A_V) - 4.20. \tag{1.11}$$

Although the NIR slope is often assumed to be consistent, even among the MW sightlines, extinction curves show variability in the IR wavelengths.

5. A_V, which reflects the dust column density or the optical depth, appears effective in expressing trends in 2175 Å bumps and UV slopes. Unlike the optical slope, as described in 3 above, A_V is more reliable in expressing the SMC and LMC curves. (Higher A_V indicates a greyer UV slope and a stronger bump.)

Although I focus on 'attenuation' curves in this dissertation, it is worthwhile recognising the variety of 'extinction' curves as the building blocks of 'attenuation' curves.

Variety of 'attenuation' curves

So far, many studies have focused on attenuation curves in the UV and optical wavelengths via both observations and simulations. The investigation in the IR is more challenging due to absorption by the earth's atmosphere and intrinsically weaker attenuation. Ascribed to the inherent complexity of attenuation curves compared to extinction curves, various trends in attenuation curves (some are even the opposite) have emerged from different methods. In Figure 1.4, I show expected trends, albeit with some ambiguity in global agreement.

A fundamental difference from 'extinction' curves is additional geometric effects must be considered when dealing with 'attenuation' curves. As the orange arrow in Figure 1.4 demonstrates, a greyer curve is expected for a more complex star-dust geometry. This trend is interpreted as a result of UV pho-
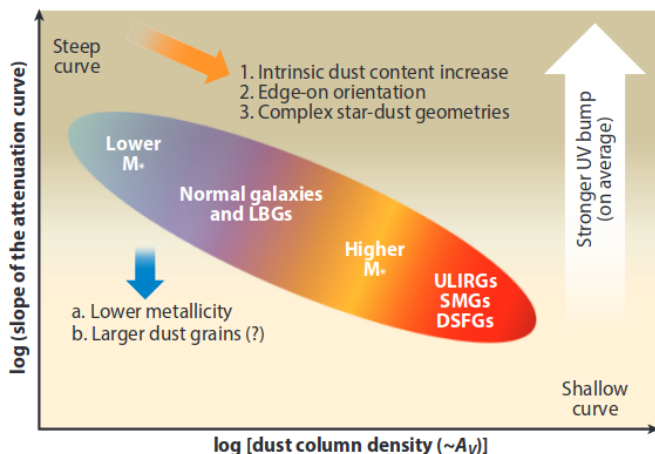
Figure 1.4. An illustration of trends between the slope of the attenuation curves and the dust column density, which is approximately the same as A_V. The oval represents the tendency that more massive galaxies to have higher dust column density (A_V) and shallower attenuation curves. Note that this is one of the proposed trends and is still under debate. The figure is taken from Salim and Narayanan (2020)

tons that more easily escape from complex star-dust distributions. In more complex geometries, i.e., in clumpier environments, some UV photons can escape the natal clouds (where young stars radiate strongly in UV) through porous-like structures, and that leads to weaker attenuation in the UV. The same arrow indicates a tendency for the curve to be shallower as A_V increases, consistent with what we discern in extinction curves.

Other than the geometric effects, dust grain properties also play a role. In a study of local (low-redshift) galaxies, a moderate trend is found that galaxies with lower metallicity have shallower attenuation curves (see the blue arrow in Figure 1.4), which could be attributed to dust grain properties. Although Shivaei et al. (2020) found an inverted trend (lower-metallicity galaxies give steeper curves), they provide

two different explanations for the correlation between metallicities and slopes: one is geometric effects and the other is dust grain property effects. They refer to a simulation study of extinction curves with dust evolution implemented (Hou et al. 2017), and highlight that small dust grains dominate in lower-metallicity environments, resulting in a steeper curve. Since dust composition (carbonaceous or silicate) also alters the dust grain size evolution, the composition of dust can also take part in the shapes of attenuation curves.

Lastly, Lo Faro et al. (2017) places the importance of attenuation curves in the NIR for estimating galaxy properties, such as stellar masses. They estimate substantially larger stellar masses for high-redshift (distant) galaxies with greyer curves in the NIR, compared to modified attenuation curves of Calzetti et al. (2000).

1.2.2 Hydrogen Balmer decrements and attenuation curves

Reddy et al. (2020) derive nebular attenuation curves of high-redshift galaxies directly based on hydrogen Balmer decrements, in contrast to most studies that derive attenuation curves by comparing observed SEDs with assumed unattenuated ones. The methodology is described in Section 2.2, but I summarise it briefly here.

They measure five Balmer emission lines ($H\alpha$, $H\beta$, $H\gamma$, $H\delta$, and $H\epsilon$) of galaxies at redshift around 2. To overcome the faintness of distant galaxies, they create composite spectra of the galaxies to measure the flux density of the lines. By calculating the ratios of these lines and evaluating deviations from the theoretically expected ratios under certain conditions, they obtain attenuation values to constrain the curve. In this study, they normalise the curve by reddening $E(B-V) = A'_B - A'_V = A_B - A_V$, and shifted to $k'(H\alpha) = 1$, as shown in Figure 1.5, where $k'(\lambda) = A'(\lambda)/E(B-V)$.

Comparing their nebular reddening (derived using Balmer decrement) with the stellar reddening (gained by SED-fitting), they directly confirm that the nebular reddening is

Figure 1.5. The attenuation curve k' derived in Reddy et al. (2020) (the blue line). This curve is normalised by reddening $E(B-V)$ and fixed to 1 at the wavelength of $H\alpha$.

larger than the stellar reddening. This is often interpreted as the difference in regions where nebular and stellar emission arises; Balmer emission lines (hydrogen recombination lines) are predominately emitted in regions where young, hot stars ionise hydrogen atoms. Because these regions tend to be dust-rich, hydrogen emission lines experience more attenuation than stellar continuum emission from stars with various ages. Recent studies suggest that young stars can still emit ionising photons even after drifting away from their parent clouds. Thus, Reddy et al. (2020) propose three possibilities for the cause of extra reddening of nebular emission. Therefore, it is important to note that nebular dust attenuation curves are likely biased towards representing more dust-rich regions in galaxies.

1.2.3 Aims of this research

The primary goals of this research are to obtain dust attenuation curves using nebular emission lines for individual galaxies and study their relationships to galaxy properties. In particular, I aim to also use hydrogen recombination lines at infrared wavelengths, which have been technically challenging to observe because the atmosphere is opaque, unlike at visible wavelengths. Now with the unprecedentedly powerful *James Webb Space Telescope* and planned infrared space telescopes designed to gaze into the universe in the IR, attenuation curves including the IR range would be desirable for capturing the true galaxy properties. Reddy et al. (2020) successfully constrain a nebular dust attenuation curve to 6564Å where Hα resides. In this work, I extend the curve towards IR, up to 4.05 μm (Brα), using the same method to each of 100 simulated galaxies generated by the dust radiation transfer software, POWDERDAY (Narayanan et al. 2021). I then investigate potential relations between the derived dust attenuation curves and various galaxy properties.

Chapter 2

Methods: Derivation of attenuation curves

2.1 Data: simulated galaxies

For this study, I analyse SEDs derived from 100 simulated galaxies generated by the POWDERDAY dust radiation transfer software (Narayanan et al. 2021). POWDERDAY offers flexibility for users to select their desired galaxy formation models to generate galaxy SEDs. Figure 2.1 schematically depicts the workflow of POWDERDAY. First, POWDERDAY uses a snapshot of a galaxy simulation to generate an unattenuated SED. This SED encompasses various emission lines, including hydrogen recombination lines. Then, POWDERDAY constructs grids to perform radiative transfer. Finally, by combining the unattenuated SED and dust treatment, it yields an attenuated SED with spectral features (Narayanan et al. 2021; Lower et al. 2022). I utilise different data from the same snapshot for wavelengths $< 1\mu m$ and $> 1\mu m$ as the data that have high resolution in shorter wavelengths presents low resolution in longer wavelengths, and vice versa. In order to efficiently perform simulations, the infrared part (> 1um) of the SED has a coarser spectral resolution than the optical part (0.3-1um).

For the purpose of this work, I measure the line luminosity of 10 hydrogen recombination lines of the attenuated SEDs. This is equivalent to what astronomers observe with a telescope. In addition to the SEDs, I extract galaxy properties (e.g. metallicity, star formation rate (SFR), various galaxy sizes, and masses) from simulated galaxies using the software. I then use these galaxy properties to compare to derived nebular dust attenuation curves.

2.2 Derivation of attenuation curves

In this section, reference is frequently made to Reddy et al. (2020) as I adopt the same method.

2.2.1 Line fitting & luminosity calculations

To derive attenuation curves, I fit 10 hydrogen recombination lines from Hδ to Brα present in the SEDs. First, I fit each line with Gaussian functions on top of a linear function. The main Gaussian function is the best fit model for the hydrogen lines from nebulae and the linear function is for the underlying stellar continuum. The secondary Gaussian function is employed to fit the absorption feature that often presents in Hδ, Hγ, Hβ, and Hα. I only fit the secondary component when the single Gaussian fit does not produce a good fit. In addition, for some galaxies which exhibit neighboring spectral lines, I add one or two more Gaussian functions to simultaneously fit all the features. Specifically, one additional Gaussian function is incorporated for Paγ and Paβ, while two are added for Hγ and Hα to accommodate neighboring lines
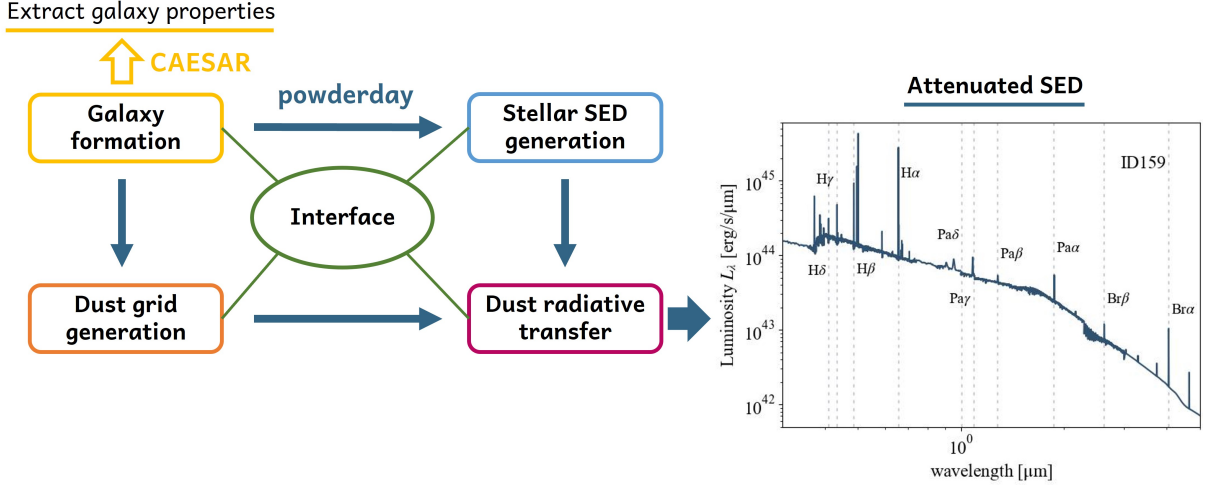
Figure 2.1. The workflow for generating attenuated SEDs from a snapshot of galaxy formation simulations. The newly released tool, POWDERDAY (the blue arrows) constructs the stellar SED (the light blue box; nebular emission lines are also considered) from galaxy formation simulations. It has the unique capability of interfacing a wide range of galaxy simulation codes. The interstellar dust geometry (the orange box; this includes dust extinction properties) from a snapshot of a galaxy formation simulation is used to propagate the light through dust radiative transfer (the magenta box) to create the attenuated SED (the right figure: an example of galaxy ID 159, with the grey dashed lines indicating the wavelengths of 10 hydrogen lines). An interface shown in the green circle facilitates the interconnection between these stages. Essential galaxy properties, such as masses and metallicity, are acquired through the CAESAR software (yellow arrow). This schematic representation is adapted from Narayanan et al. (2021).

Line	Peak (μm)	Fitting window (μm)	Neighbouring lines (wavelength)	Galaxy ID without absorptions
Hδ	0.4103	0.4033–0.4173	–	43, 66, 124
Hγ	0.4342	0.4250–0.4450	OII (0.4317 μm) OIII (0.4364 μm)	43
Hβ	0.4863	0.4857–0.4950	–	–
Hα	0.6565	0.6475–0.6650	NII (0.6585 μm, 0.6549 μm)	12, 38, 51, 56, 73, 99, 111, 120, 133, 142, 148, 151
Paδ	1.005	0.9553–1.055	–	–
Paγ	1.094	1.070–1.120	HeI (1.083 μm)	–
Paβ	1.282	1.232–1.332	FeII (1.257 μm)	–
Paα	1.876	1.826–1.926	–	–
Brβ	2.626	2.576– 2.676	–	–
Brα	4.052	4.002– 4.102	–	–

Table 2.1. Hydrogen recombination line fitting parameters.
Peak: The peak wavelength of each hydrogen recombination line used in this research. Fitting window: The wavelength range employed for the line fitting process.
Neighbours: The adjacent lines that are simultaneously fitted along with the main lines.
Galaxy ID without absorption: The galaxy IDs where fitting was conducted without considering absorption for Hδ, Hγ, Hβ, and Hα.

(see Table 2.1). I utilise LMFIT, a Python-based tool for non-linear least-squares minimization and curve-fitting[1], to perform the fitting.

LMFIT provides optimal parameter values (p_0, p_1, and p_2) together with their estimated standard errors in the main Gaussian equation:

$$p_0 \times \exp\left[-\left(\frac{\lambda - p_1}{p_2}\right)^2 \cdot 2(2\ln 2)\right],\tag{2.1}$$

where p_0, p_1, and p_2 represent the peak strength of the line, the center wavelength of the line, and the full width of half maximum (FWHM), respectively. I calculate the line luminosity by analytically integrating this equation. For the calculation of error propagation, I use the analytical form of this integration:

$$p_0\sqrt{\frac{\pi}{2(2\ln 2)}} \times p_2.\tag{2.2}$$

To ensure a robust analysis, I only employ lines with a signal-to-noise ratio $S/N > 3$ among all lines. Some emission lines are too faint to make this S/N cut, but this criterion ensures the reliability of the derived attenuation curves.

2.2.2 Calculation of attenuation of each line

We can rewrite Equation (1.1) in terms of fluxes or luminosity as:

$$-2.5\log_{10} f(\lambda) = -2.5\log_{10} f_0(\lambda) + A(\lambda),\tag{2.3}$$

or

$$f(\lambda) = f_0(\lambda) \times 10^{-0.4 \times A(\lambda)},\tag{2.4}$$

where $f(\lambda)$ is the measured flux and $f_0(\lambda)$ is the intrinsic (unattenuated) flux of the line centred at λ. To examine the attenuation, I take flux ratios of Brα[2] to another hydrogen line at λ:

$$\frac{f(\text{Br}\alpha)}{f(\lambda)} = \frac{f_0(\text{Br}\alpha)}{f_0(\lambda)} \times 10^{-0.4 \times [A(\text{Br}\alpha) - A(\lambda)]}.\tag{2.5}$$

Then the attenuation $A(\lambda)$ can be written as:

$$A(\lambda) = 2.5\left[\log_{10}\left(\frac{f(\text{Br}\alpha)}{f(\lambda)}\right) - \log_{10}\left(\frac{f_0(\text{Br}\alpha)}{f_0(\lambda)}\right)\right] + A(\text{Br}\alpha).\tag{2.6}$$

However, because A(Bra) is unknown initially, I newly define the attenuation A'(lambda) as

$$A'(\lambda) \equiv A(\lambda) + [1 - A(\text{Br}\alpha)],\tag{2.7}$$

---

[1] https://lmfit.github.io/lmfit-py/index.html

[2] I choose Bra for this work because it is at the longest wavelength available, but any other lines could be chosen

13

where $A'(\lambda)$ is the shifted attenuation by a constant $1 - A(\text{Br}\alpha)$. Thus, the final expression of the attenuation I calculate becomes:

$$A'(\lambda) = 2.5 \left[\log_{10} \left(\frac{f(\text{Br}\alpha)}{f(\lambda)} \right) - \log_{10} \left(\frac{f_0(\text{Br}\alpha)}{f_0(\lambda)} \right) \right] + 1. \tag{2.8}$$

To account for uncertainties, I calculate the standard errors of $A'(\lambda)$ through error propagation.

For intrinsic line flux ratios $f_0(\text{Br}\alpha)/f_0(\lambda)$, I employ theoretically calculated hydrogen recombination line intensities relative to $H\beta$ (Table 2.2), under Case B conditions with a typical temperature $T = 10^4$ K and electron density $n_e = 10^2$ cm^{-3} as in Reddy et al. (2020). There are two main types of assumptions for the behaviours of high-energy photons in gaseous nebulae: Case A and Case B (Osterbrock and Ferland 2006). Case B assumes an optically thick environment, and every Lyman photon corresponds to a transition from $n \geq 3 \rightarrow 1$, where n is the principal quantum number, is converted to lower-series photons, such as Balmer ($n \rightarrow 2$) and Paschen ($n \rightarrow 3$) series, and Lyα or two-continuum photons (both correspond to $2 \rightarrow 1$ transitions) while they are repeatedly scattered before escaping from the nebula. In Case A, on the other hand, it assumes that the nebula is optically thin and allows Lyman photons to escape from the nebula without being scattered and converted to lower energy photons. Since hydrogen recombination lines predominantly come from regions where ionised hydrogen is abundant, such as in star-forming clouds, Case B is a more significant component than Case A in the observed luminosity. In addition to thermodynamic equilibriums from which the hydrogen line ratios are calculated, collisional transitions depending on n_e are also taken into account for the values shown in Table 2.2.

Table 2.2. Theoretical HI recombination line ratios to $H\beta$ for Case B with $T = 10^4$ K and $n_e = 10^2$ cm^{-3} (Osterbrock and Ferland 2006).

Line	Intensity relative to $H\beta$
$H\delta$	0.259
$H\gamma$	0.468
$H\alpha$	2.863
$Pa\delta$	0.0555
$Pa\gamma$	0.0904
$Pa\beta$	0.163
$Pa\alpha$	0.339
$Br\beta$	0.0455
$Br\alpha$	0.0802

2.2.3 Calculation of attenuation curves

With the $A'(\lambda)$ value at each hydrogen recombination line and their associated errors in hand, I fit the $A'(\lambda)$ data points for each galaxy with a quadratic-in-$1/\lambda$ equation:

$$a_0 + \frac{a_1}{\lambda} + \frac{a_2}{\lambda^2} \tag{2.9}$$

This equation is consistent with one of the functions fitted in Reddy et al. (2020). I do not use their other function, which is a linear expression, in this work as it results in a uniformly normalised attenuation curve for all individual galaxies. Using LMFIT, I iterate the following steps 10000 times in a Monte Carlo fashion.

First, for galaxies with more than four $A'(\lambda)$ data points, I sample uniformly randomised $A'(\lambda)$ points for each line within the 1σ error range, and fit with Equation (2.9). I exclude $A'(\text{Pa}\beta)$ data points from this fit given their consistently elevated values in many sample galaxies. Although the excess in $A'(\text{Pa}\beta)$ may suggest some physical importance in the dust attenuation feature, I prioritize a broader understanding of the shapes of attenuation curves in this study.

Second, I shift the $A'(\lambda)$ curve back to the $A(\lambda)$ curve (see Equations (2.6) and (2.7)). Based on the infrared interstellar extinction measured by Rieke and Lebofsky (1985), the V-band normalized attenuation

at 13 μm is 0.027, $A(13um)/A_V = 0.027$. I then calculate the shift, C, to apply to $A'(\lambda)$:

$$C = \frac{0.027A'(V) - A'(13\mu m)}{1 - 0.027}. \tag{2.10}$$

Now $A(\lambda) = A'(\lambda) + C$ can be considered as the tentative dust attenuation without any normalizations.

Third, I calculate the reddening, $E(B-V) = A(B) - A(V)$, using the values $A(B)$ and $A(V)$ on the derived tentative $A(\lambda)$ curve and normalise the tentative $A(\lambda)$ data points by $E(B-V)$ to obtain the tentative $k(\lambda)$ data points:

$$k(\lambda) = \frac{A(\lambda)}{E(B-V)} \tag{2.11}$$

After the iteration of these steps above, I extract the medians of $A(\lambda)$ and $k(\lambda)$ data points at each line and obtain the final $A(\lambda)$ curve by fitting the 200 linearly spaced data points over the 0.35–5.0 μm range. The errors of $A(\lambda)$ and $k(\lambda)$ points are defined as 1σ, while for the $A(\lambda)$ curve, I took the 2.5th and 97.5th percentiles at each of the 200 linearly spaced wavelengths.

Finally, I fit again the $k(\lambda)$ data points with the same quadratic equation with a similar Monte Carlo approach to derive the attenuation curve normalised by $E(B-V)$. Adopting the same procedure as before for deriving the $A(\lambda)$ curve, I randomly sample $k(\lambda)$ data points at each line within their 1σ ranges, and fit with Equation (2.9). I extract the medians of the $k(\lambda)$ values at each of the linearly spaced 200 wavelengths for its median curve, and the 2.5th and 97.5th percentiles for the error of the fitted curve.

To compare with the attenuation curve derived by Reddy et al. (2020), I shift the $k(\lambda)$ curve to $k'(\mathrm{H}\alpha) = 1$ as defined by them. It is important to note that a direct comparison with Reddy et al. (2020) is not straightforward due to different assumptions in how to shift the curve (Equation (2.10)). While Reddy et al. (2020) assumes $k(2.8\mu m) = 0$, my work assumed the presence of some attenuation at Brα (4 μm).

2.2.4 Another attenuation curve: A_λ/A_V

The direct comparison of attenuation curves poses challenges, as highlighted in Section 1.2.1. To facilitate a more interpretable characterization of the derived curves, I opt to use the optical slope and the NIR slope shown in Equations (1.7) and (1.9), respectively. Because these parameters are derived from the attenuation curve normalized by $A(V)$, this is written as:

$$\frac{A(\lambda)}{A(V)}. \tag{2.12}$$

Applying the same method employed above, I conduct this normalisation for each iteration by replacing Equation (2.11) with Equation (2.12) to derive this form of attenuation curves.

2.3 Attenuation curves and their characterization

To effectively characterize the attenuation curves, I focus on two parameters: the optical slope (A_B/A_V) and the NIR slope (β_{NIR}). Additionally, I adopt $A_{2\mu m}/A_{4\mu m}$ to further investigate the IR range of the attenuation curve. For both A_B/A_V and $A_{2\mu m}/A_{4\mu m}$, I calculate the median values and the 15.87th and 84.13th percentiles during the iterative process for the $A'(\lambda)$ curve fitting. For the calculation of β_{NIR}, I perform another fit to a tentative A_λ/A_V curve with Equation (1.9): I use the fitted curve of Equation

(2.9) over the range 0.9–5 μm, and fitted Equation (1.9). Then, I calculate the median and the 15.87th and 84.13th percentile values of β_{NIR}.

Chapter 3

Results

3.1 Fits of hydrogen recombination lines

In Figure 3.1, I show the results of fitting hydrogen recombination lines of the galaxy, ID 159, as an example. The number of galaxies in which each line is detected is listed in Table 3.1. Paδ and Paγ are not detected in any of the galaxies, and the largest number of line detections in a single galaxy is eight, Hδ, Hγ, Hβ, Hα, Paβ, Paα, Brβ, and Brα. Encouragingly, Brα is detected in all of the galaxies so that additional treatments in the attenuation calculations are not needed (see Equation (2.8)).

The top three most and least luminous galaxies for each line are also listed in Table 3.1. A distinctive difference is seen between short-wavelength lines (Hδ to Hα) and long-wavelength lines (Hα to Brα) in the top three most luminous galaxies, already implying some variations in dust attenuation curves. If all galaxies follow the same attenuation curve, the same set of galaxies should have the most luminous lines at both short- and long-wavelengths. Although Hδ and Hγ are not detected in ID 18, which has strong lines in Paα to Brα, all of the eight lines are available in ID 131, 47, 78, 34, and 70.

Listed in Table 3.2 are the counts of galaxies with available lines. As I mentioned in Section 2.2.3, because Paβ is excluded from the $A'(\lambda)$ fitting, I also list the counts when Paβ is excluded. Given the three free parameters in the fitting curve equation (see Equation (2.9)), a galaxy must possess at least four available lines to create the attenuation curve. This results in 76 galaxies for creating quadratic fitted attenuation curves.

3.2 Derived dust attenuation curves

The derived dust attenuation curves directly from the simulated galaxies exhibit considerable variability, in contrast to the commonly assumed fixed curve (see Figure 3.2). A significant number of galaxies turn out to have $A(\lambda)$ curves that start rising between 0.35–5.00 μm, with some even displaying greater attenuation at Brα than at Hα, These non-monotonic curves have been excluded in the following analyses to maintain analytical clarity, unless explicitly stated otherwise.

In Figure 3.2a and 3.2b, I show $A(\lambda)$ curves before any normalisations. The curves in Figure 3.2a have effectively captured the measured $A(\lambda)$ points well. However, there may be a systematic offset in the IR range. We see a diversity of the curves across the whole wavelength range, particularly at shorter wavelengths than at longer wavelengths (Figure 3.2b). Curves with $\beta_{\mathrm{NIR}} > 1.5$ (shown by the dark pink in Figure 3.2b) tend to show small $A(B)$ and $A(V)$ values, except for the one displaying a steep slope in the visible light region with moderate $A(V)$. Note that the $A(\lambda)$ curves have been shifted to $A(13\mu\mathrm{m}) = 0.027$

Table 3.1. The number of galaxies in which each line is used in the calculation of its attenuation. I also listed the result for Paβ to show that this line is detected in some galaxies, albeit I did not use this line for the attenuation calculation (see Section 2.2.3 for the details). Additionally, the top three most and least luminous galaxies for each line are shown, together with their respective luminosities.

| Line	Number of detection	Most luminous (descending)		Least luminous (ascending)	
		ID	Luminosity (10^{40} erg/s)	ID	Luminosity (10^{39} erg/s)
Hδ	44	131	9.690 ± 0.333	158	5.531 ± 0.480
		47	9.171 ± 0.545	118	7.316 ± 1.962
		78	8.209 ± 0.332	115	8.464 ± 1.855
Hγ	60	131	19.89 ± 0.32	124	5.285 ± 1.599
		47	18.80 ± 0.51	143	5.416 ± 1.085
		78	15.98 ± 0.29	125	6.833 ± 1.071
Hβ	75	47	48.96 ± 0.44	127	5.573e ± 0.817
		131	48.93 ± 0.23	142	6.349e ± 0.973
		15	41.03 ± 0.53	38	8.870 ± 2.774
Hα	83	131	153.3 ± 1.9	95	8.023 ± 1.552
		47	152.9 ± 4.7	76	13.78 ± 4.04
		70	138.5 ± 5.4	81	22.23 ± 1.14
Paδ	0	–	–	–	–
Paγ	0	–	–	–	–
Paβ	48	34	7.054 ± 0.862	99	4.232 ± 1.389
		70	6.421 ± 0.854	158	4.272 ± 0.465
		159	6.365 ± 0.276	83	5.591 ± 1.562
Paα	79	34	20.75 ± 0.84	142	4.839 ± 1.142
		70	18.85 ± 0.80	143	7.291 ± 1.890
		18	18.61 ± 1.11	91	7.429 ± 1.499
Brβ	63	34	2.940 ± 0.343	120	1.334 ± 0.414
		18	2.678 ± 0.404	158	1.345 ± 0.129
		70	2.603 ± 0.320	99	1.571 ± 0.356
Brα	100	34	5.785 ± 0.005	46	0.059 ± 0.010
		18	5.412 ± 0.007	153	0.086 ± 0.002
		70	5.054 ± 0.004	129	0.131 ± 0.005
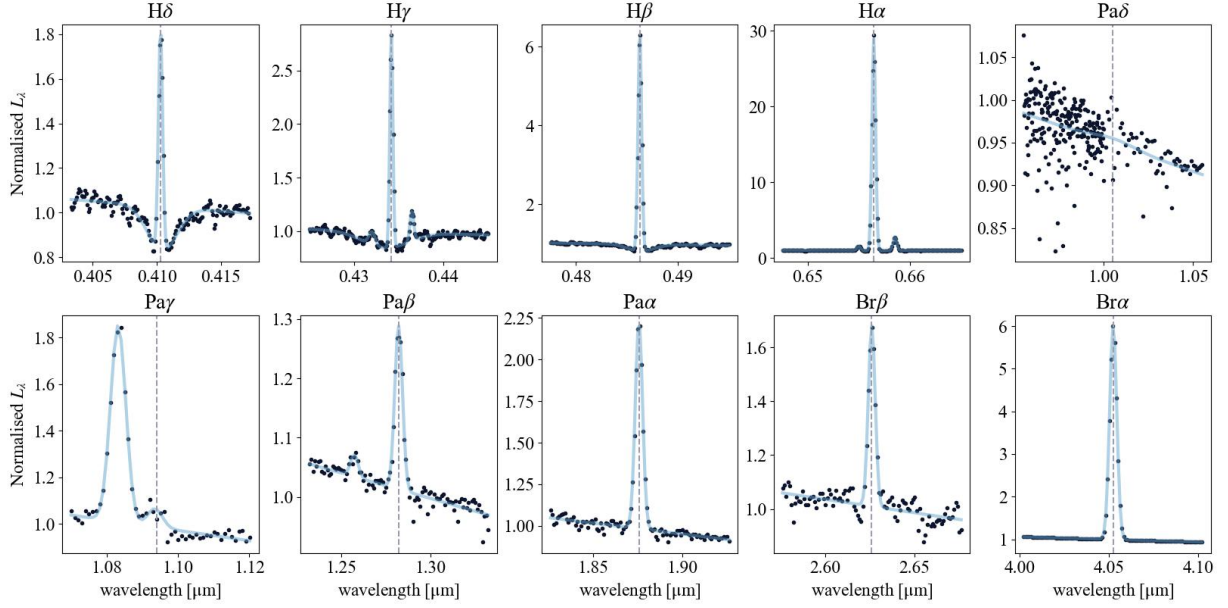
Figure 3.1. An example of the fitting results for the 10 hydrogen recombination lines, from Hδ to Brα in the galaxy ID 159. The black data points represent the spectrum of the galaxy, and the light blue lines show the results of the fitted Gaussian function(s). The dashed grey lines indicate the peak wavelength for each line (Table 2.1).

(Equation (2.10)) although the appropriateness of this normalization for every galaxy remains uncertain.

The $k'(\lambda)$ curves (Equation (2.11)) are shown in Figure 3.2c and 3.2d. At the shorter wavelengths from Hδ to Hα, all the curves from this work and the references curves, Reddy et al. (2020) and Calzetti et al. (2000) successfully reproduce the $k'(\lambda)$ values. However, a simple extrapolation of these reference curves produces much lower $k'(\lambda)$ at longer wavelengths (from Paα to Brα), while the curve from this work aligns closely with the measured $k'(\lambda)$ points. This pattern is also discerned in individual galaxies, as illustrated in Figure 3.2d, in which I overplot all derived monotonic (non-rising) $k'(\lambda)$ curves. The normalization with $E(B-V)$ in the optical emphasizes the diversity of the curves in the NIR. Galaxies with $\beta_{\mathrm{NIR}} > 1.5$ show a sharper change from the optical to NIR range, and neither the Reddy et al. (2020) nor Calzetti et al. (2000) curves agree with them in this range.

Table 3.2. The first column is the number of hydrogen recombination lines in a galaxy, and the second and the third columns display the number of galaxies with that specific count of hydrogen lines, with and without Paβ, respectively.

Lines	Number of galaxies (with Paβ)	Number of galaxies (without Paβ)
1	17	17
2	3	3
3	5	5
4	7	7
5	10	13
6	11	12
7	6	43
8	41	0

The normalisation by $A(V)$ amplifies the difference between the $\beta_{\mathrm{NIR}} > 1.5$ and < 1.5 curves seen $k'(\lambda)$ (Figure 3.2f). This division aligns with the distribution in the $\beta_{\mathrm{NIR}} - A_B/A_V$ relation shown in Figure 3.3a. In galaxies of this study, a constant trend of a larger β_{NIR} with a large A_B/A_V has been observed. Interestingly, both types of the curves ($\beta_{\mathrm{NIR}} > 1.5$ and < 1.5) appear to have lower β_{NIR} at a given A_B/A_V compared to the MW extinction curves. This discrepancy could be attributed to differences between
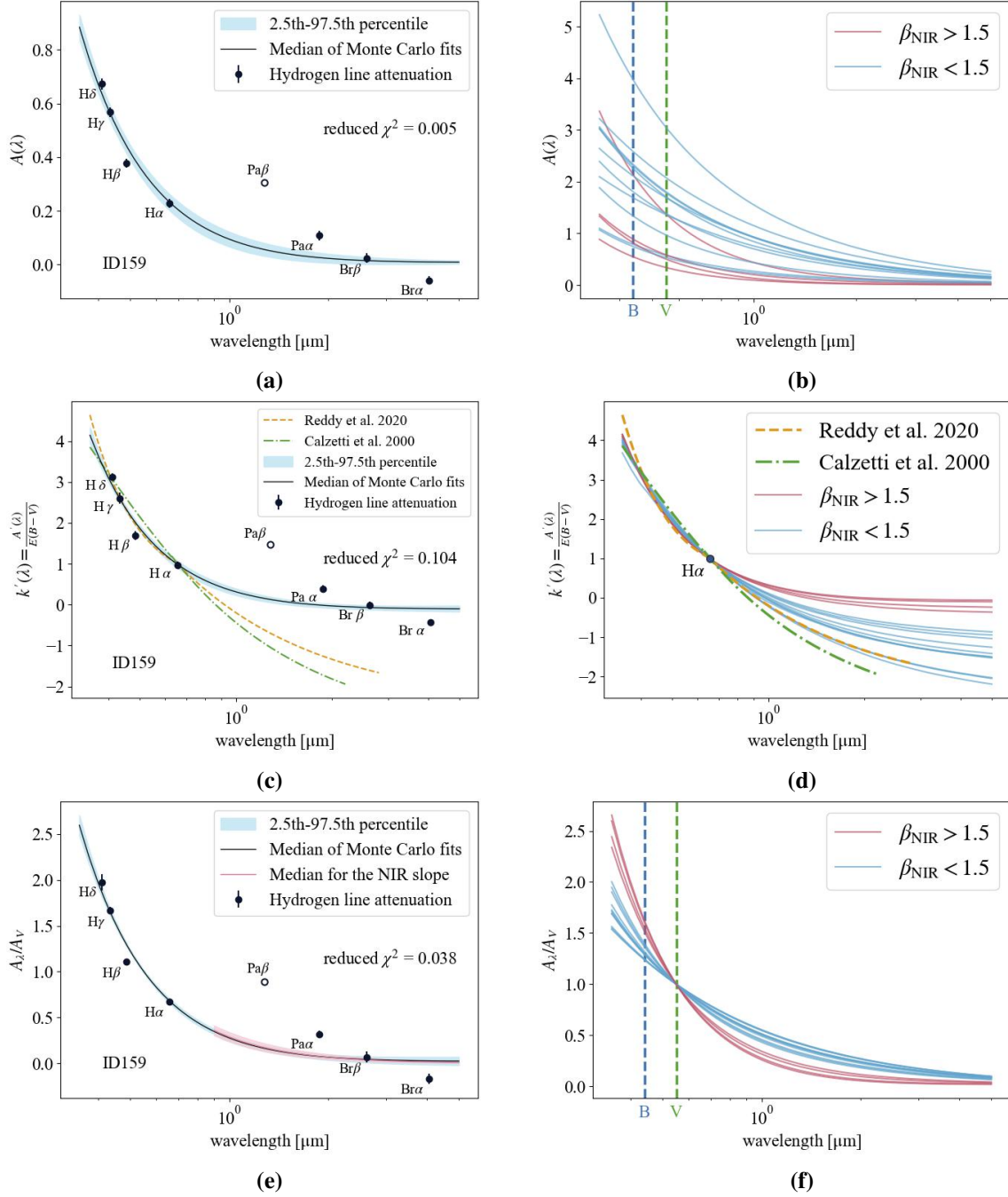
Figure 3.2. (a),(c), and (e): The $A(\lambda)$, $k'(\lambda)$, and A_λ/A_V curve fittings for ID 159, respectively. The data points correspond to the attenuation values at each hydrogen line, and the black lines are the median curves from Monte Carlo fits with the 2.5th–97.5th percentile denoted by the light blue area. The Paβ data point is shown as an empty circle to indicate that it is not used for the fittings (see Section 2.2.3). The pale pink line and area in (e) are the result of the fit for the NIR slope (Equation (1.9)). (b), (d), and (f): The light blue and dark pink lines are the monotonic $A(\lambda)$, $k'(\lambda)$, and A_λ/A_V median curves, respectively for individual galaxies whose curves are derived. The light blue lines are the curves with $\beta_{NIR} < 1.5$ and the dark pink represents the galaxies with $\beta_{NIR} > 1.5$ (see Figure 3.3a). In (b) and (f), the wavelengths in the B (0.44 μm) and V (0.55 μm) bands are displayed by the vertical dashed blue and green lines, respectively. All lines in (d) are shifted to $k'(H\alpha) = 1$ shown in the black circle, for normalization. The attenuation curves of Reddy et al. (2020) and Calzetti et al. (2000) are shown by the dashed yellow line and dashed-dotted green line, respectively, for comparisons in (c) and (d).
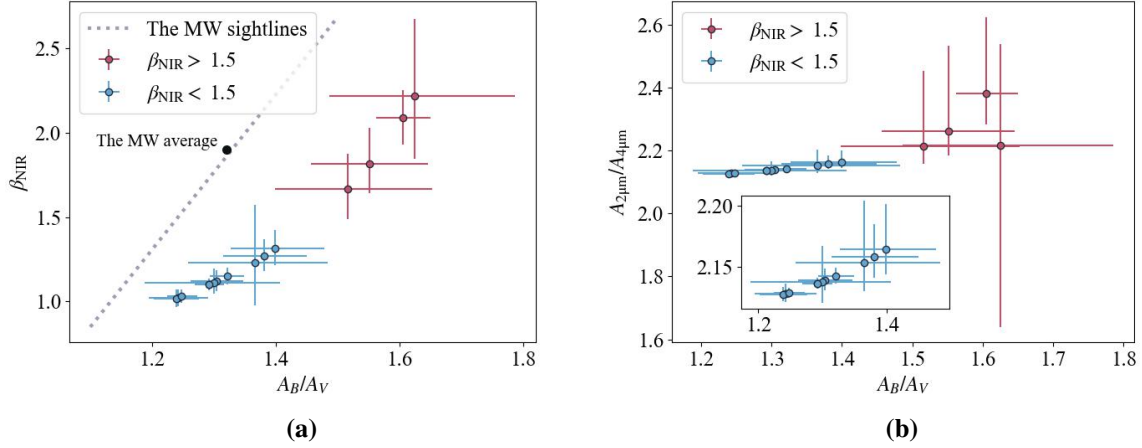
Figure 3.3. (a) and (b) show the β_{NIR} vs. A_B/A_V and $A_{2\mu m}/A_{4\mu m}$ vs. A_B/A_V plots for the monotonic curves, respectively. The curves with $\beta_{\mathrm{NIR}} < 1.5$ and > 1.5 are denoted by the light blue and the dark pink, respectively. The error bars are between the 15.87–84.13th percentiles. The black point and the dotted grey line in (a) are from Salim and Narayanan (2020) (see also Figure 1.3b) and represent the MW average and the MW sightlines, respectively (Equation (1.11)).

attenuation and extinction. Attenuation includes scattered-back light entering the sightline, potentially resulting in smaller $A(V)$ and larger A_B/A_V.

The $A_{2\mu m}/A_{4\mu m}$ ratio shown in Figure 3.3b appears to exhibit a weak correlation with A_B/A_V. This may be mirroring the $\beta_{\mathrm{NIR}} - A_B/A_V$ relation for the curves with $\beta_{\mathrm{NIR}} < 1.5$. The trend is unclear for the curves with $\beta_{\mathrm{NIR}} > 1.5$ due to their large measurement errors.

3.3 Attenuation curves and galaxy properties

While the relations between attenuation curves and galaxy properties remain a subject of ongoing discussion, as introduced in Section 1.2.1, some correlations are expected (e.g., Lower et al. 2022). I first explore relations to various masses, mass ratios, and SFR, as illustrated in Figure 3.4–3.6. For the masses, I use baryon mass (total masses excluding dark matter mass), stellar mass, gas mass, and dust mass. I also take ratios of dust-to-gas, dust-to-stellar, and dust-to-metal. Finally, SFR and specific SFR (sSFR; SFR divided by stellar mass) are explored. However, none of these parameters show any obvious correlation with the optical or NIR slopes of the derived curves.

I also examine a relation with galaxy size expressed in radius for baryon mass, as shown in Figure 3.7. There may reveal a weak correlation that galaxies with smaller radii show steeper attenuation slopes. This is in particular visible in panel (d) that shows the relation between A_B/A_V and the radius of baryon mass. In fact, the Pearson correlation coefficient for this relation is the most significant ($r = -0.588$). Furthermore, the relations to β_{NIR} and $A_{2\mu m}/A_{4\mu m}$ also show a comparable coefficient value. I also fitted with a constant ($y = a$) for each slope. Although each slope's χ^2 is smaller in the fit with the linear function than in the fit with the constant value, neither result is statistically significant. To confirm the correlation, more galaxies are needed. In particular, if galaxies with steep attenuation curves are more prevalent, there could be a correlation. On the other hand, if galaxies with large radii and steep attenuation curves are found, the correlation would be unlikely.
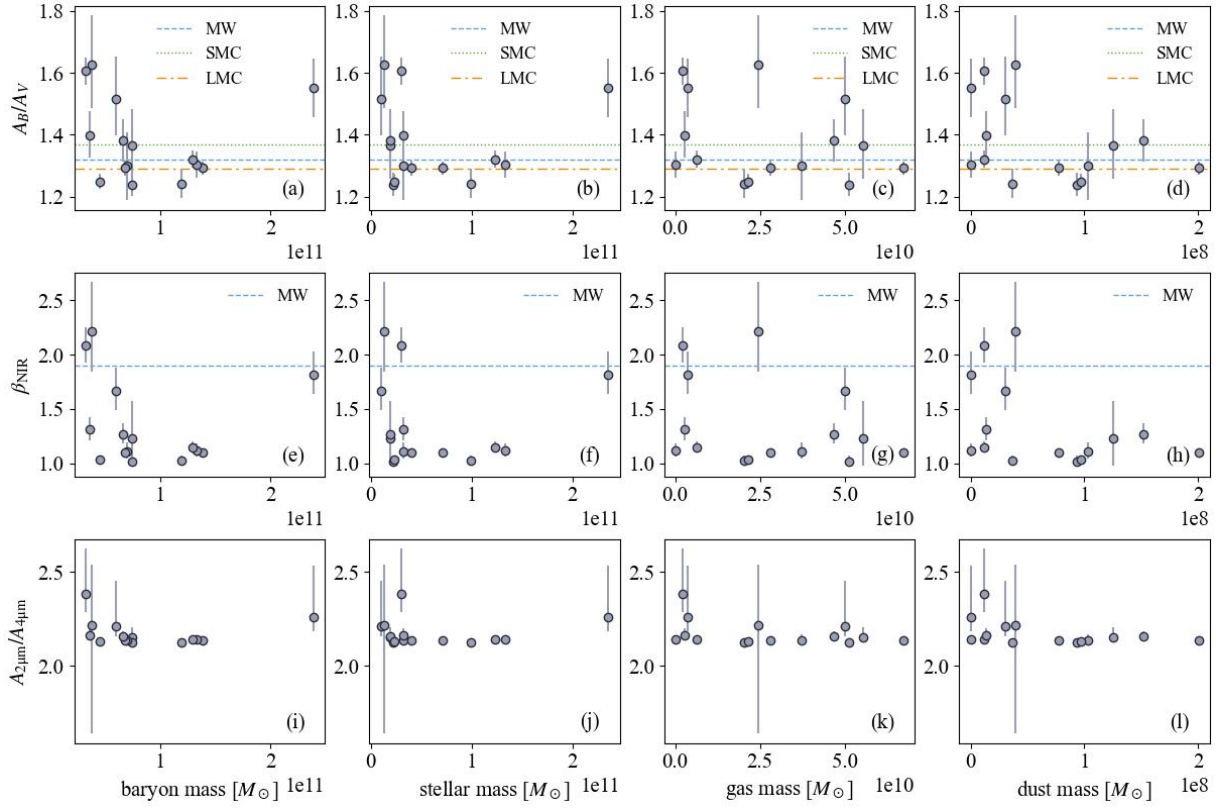
Figure 3.4. Comparisons between attenuation curve slopes (A_B/A_V, β_{NIR}, $A_{2\mu m}/A_{4\mu m}$) and baryon, stellar, gas, and dust masses. In the top 4 panels (a)–(d), A_B/A_V values of the MW, the SMC, and the LMC are presented with horizontal dashed blue, dotted green, and dash-dotted yellow lines, respectively, and β_{NIR} of the MW is shown in (e)–(h).
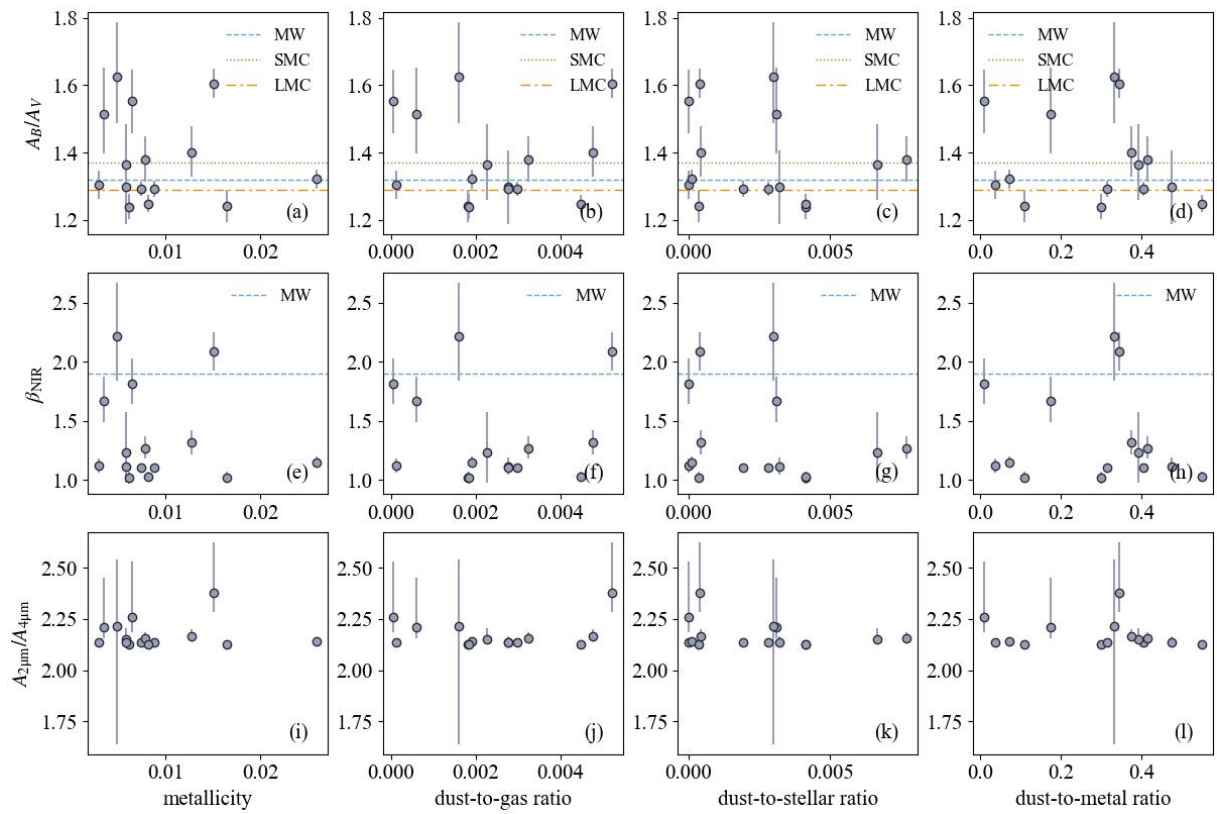
Figure 3.5. Same as Figure 3.4, except for the galaxy properties to be compared to: metallicity, dust-to-gas ratio, dust-to-stellar ratio, and dust-to-metal ratio.
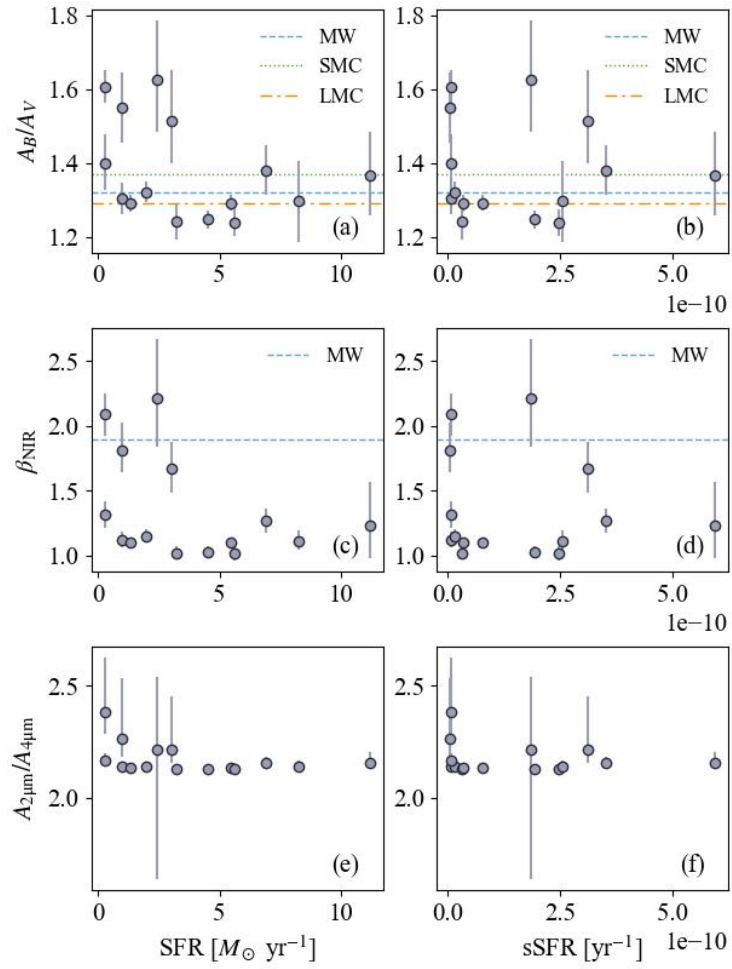
Figure 3.6. The attenuation curve slopes compared to SFR and specific SFR.
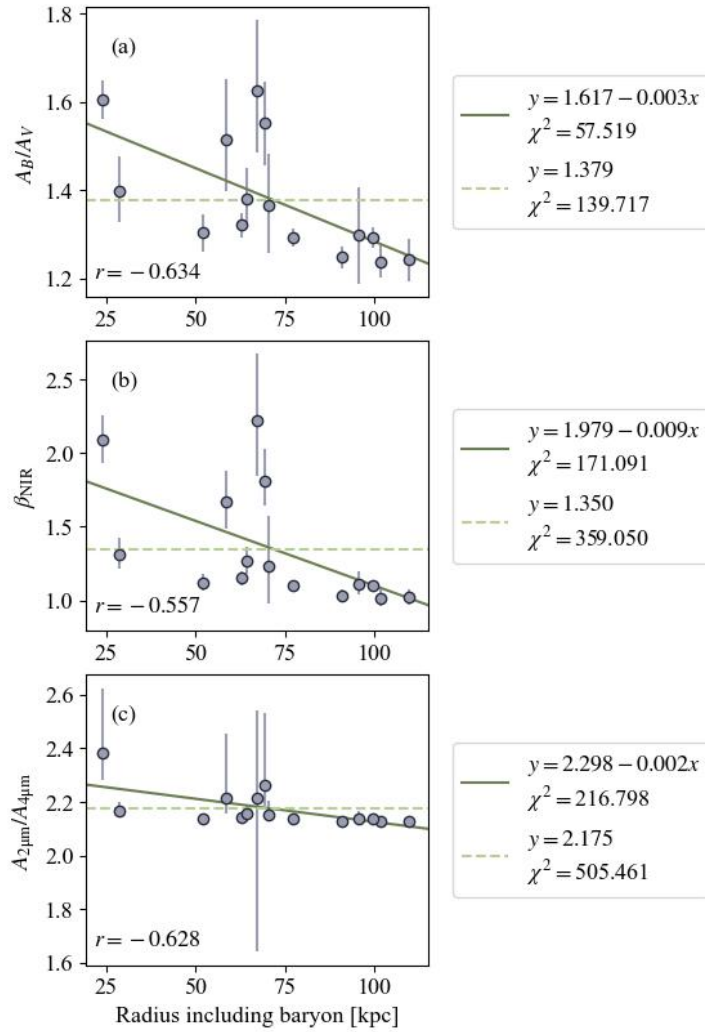
Figure 3.7. (a)–(c): The attenuation curve slopes compared to galaxy radial size. At the bottom left of each panel, the Pearson correlation coefficient (r) is shown.

Chapter 4

Discussion

4.1 Attenuation curves and galaxy properties

When exploring direct relations between dust attenuation curves and galaxy properties such as mass, mass ratios, and star formation rates, I do not find any obvious correlations. One plausible explanation for the absence of the correlations could be attributed to a limitation of the current version of the simulation. As mentioned in Section 1.2.1, there are two main factors that should be taken into account when examining attenuation curves: geometric effects and dust grain properties. The POWDERDAY simulation meticulously treats the former through radiative transfer. The dust size effects are included via spatially varying models of dust content. However, as indicated by Narayanan et al. (2021), the planned incorporation of evolving grain size distributions within a galaxy could model a more realistic underlying dust extinction curve in future versions. As both dust and galaxy properties are expected to change with galaxy growth, evolving grain size distributions may influence the observed attenuations of galaxies. If grain size distributions play a major role in shaping galaxy attenuation and properties, we may find correlations between them.

Another possibility could be caused by using hydrogen recombination lines to derive attenuation curves. Hydrogen recombination lines arise from highly ionized nebular regions where newly born hot stars reside. Because they are localised in star-forming regions, their environments are expected to be similar. This localised effect could result in attenuation curves that reflect more immediate nebular properties rather than the global characteristics of the galaxy.

On the other hand, although more samples are necessary, there may be a weak negative correlation between galaxy size and attenuation curves. If this relation can be confirmed, there are two tentative explanations. One is that the shorter light path lengths in smaller radius galaxies may lead to thinner optical depths, resulting in relatively small A_V and steeper curves (see Section 3.2 for the relation between A_V and steepness of the curve). The other explanation could be that despite galaxies being large with long light path lengths, if they tend to host clumpy dust geometries, light can escape more easily, leading to shallower attenuation curves. In addition, a dust clump tends to be dusty and may significantly attenuate IR lines, yielding shallower $A'(\lambda)$ (before shifting and normalisation) curves. Note that A'(lambda) is not affected by the assumed $A(13\mu m)/A_V = 0.027$ (Rieke and Lebofsky 1985) for any normalization. I need to adopt this assumption for every galaxy to obtain $A(V)$ for derivations of the optical NIR slopes, but if this assumption is not universal, normalized $A(V)$ could vary from the true one.
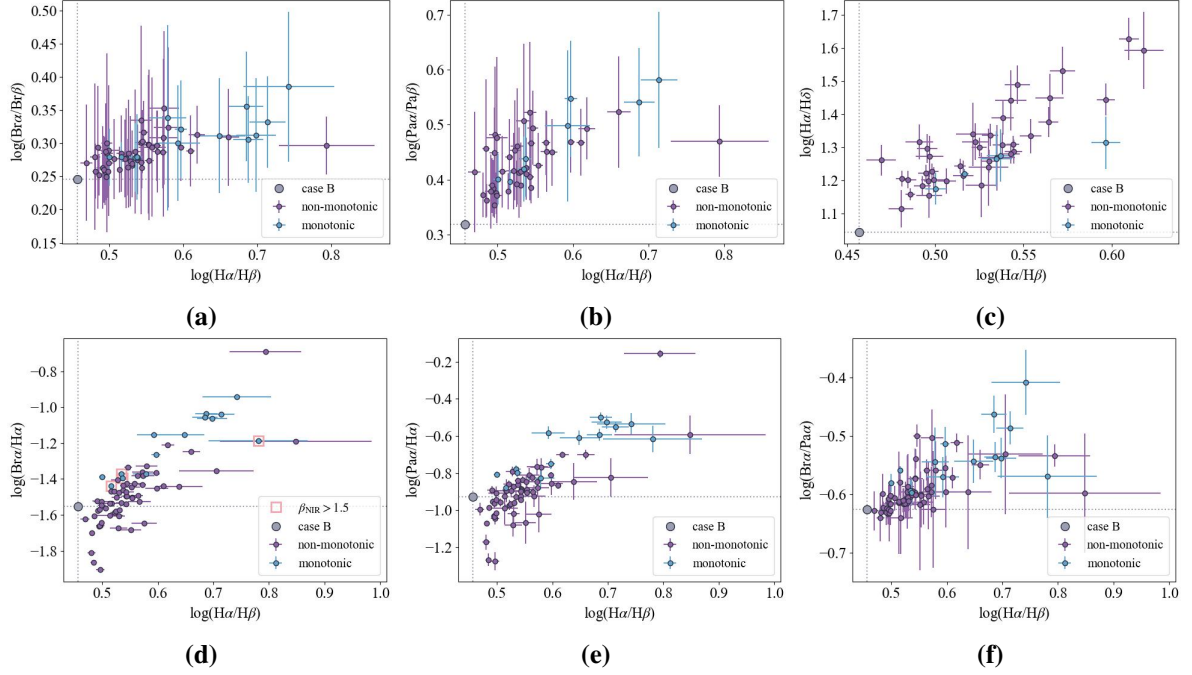
Figure 4.1. Hydrogen line ratios against $\log(H\alpha/H\beta)$. The light blue points are galaxies with monotonic attenuation curves in this study, the purple points are galaxies with non-monotonic curves which are not used in Sections 3.2 and 3.3. The grey point and dotted lines in each panel indicate the theoretical value assuming Case B (Table 2.2). The y-axes of the panels in the top row ((a)–(c)) are the line ratios between the same hydrogen line series, whereas panels in the bottom row ((d)–(f)) are for different series. In panel (a), I highlight some of the monotonic curves; the pink circles represent the galaxies with attenuation curves showing $\beta_{NIR} > 1.5$.

4.2 Monotonic vs. non-monotonic attenuation curves

Here, I revisit the galaxies with non-monotonic attenuation curves and an increase in the NIR. They are not shown in the main part of this dissertation because the attenuation is not expected to increase with wavelength. A large number of galaxies with non-monotonic curves limit my dataset size. To illustrate differences between monotonic and non-monotonic curves, I directly compare their hydrogen line ratios, as shown in Figure 4.1.

Comparing line ratios within the same series (i.e., transitions to the same level n [1]), the monotonic and non-monotonic curves populate similar scattering patterns with none of the galaxies falling below the Case B theoretical value (Figures 4.1a, 4.1b, and 4.1c). However, when considering line ratios between different series, some notable differences emerge. Some galaxies with non-monotonic curves exhibit lower line ratios than Case B, while monotonic curves remain within expected limits (Figures 4.1d, 4.1e, and 4.1f). In particular, the non-monotonic population appears to separate from the monotonic one in line ratios $\log(Br\alpha/H\alpha)$ (panel (d)) and $\log(Pa\alpha/H\alpha)$ (panel (e)). This suggests a potential influence on the observed rise in attenuation curves in the NIR range. In other words, $Br\alpha/H\alpha$ line ratios that are smaller than the Case B value are equivalent to $A(Br\alpha) > A(H\alpha)$.

Related to the non-monotonic curves, the $Br\alpha/H\alpha$ line ratios of the monotonic curves with $\beta_{NIR} > 1.5$ lie between the line ratios of the monotonic and non-monotonic curves (Figure 4.1d).

---

[1] The transitions of the Balmer series are $n \to 2$, the Paschen series are $n \to 3$, and the Bracket series are $n \to 4$.

This suggests that non-monotonic curves may represent extreme cases of these shallow attenuation curves.

However, the behaviour of lower $\log(\text{Br}\alpha/\text{H}\alpha)$ than Case B raises intriguing questions, as attenuation typically decreases at longer wavelengths unless under special conditions. One potential explanation is the observed hydrogen lines originate from varying depths within nebulae. Under the Case B condition (optically thick in the Lyman lines), higher-order Lyman photons ($n \geq 3$) are converted to lower series photons before escaping from the nebula. For example, a Lyβ photon can be converted to Hα and two-photon continuum to escape, and a Lyγ photon can produce Paα and Hβ in addition to Hα, to reach outside of a nebula.

Emission lines from longer wavelengths allow them to reach further from the denser inner nebula region. As illustrated in Figure 4.2, photons from the same series but lower order (longer wavelength) originating from the outer nebula may be less absorbed or scattered along pathways, being less sensitive to attenuation. Thus, attenuation for lower-series photons may depend on the distance that the Lyman photons can travel. For instance, if Balmer or Paschen lines also become optically thick as the dust cloud becomes deeper, lower-order series lines may only be emitted from surface of the cloud.

There is a caveat in this interpretation. In contrast to the expectation from a stratified dust cloud, some galaxies show Hγ/Hδ ratios smaller than in the Case B condition(see the Appendix). However, this could be due to poorly fitted Hγ emission because of the neighboring Ca I absorption line at $0.4307\,\mu$m. An underestimate of absorption would decrease the emission line flux and increase the $A(\text{H}\gamma)$ from their true values.

Figure 4.2. Schematic view of a possible structure of a dense cloud and hydrogen recombination lines. Emission lines caused by lower-order Lyman photons come from the entire clouds, while emission lines converted from higher-order Lyman photons are emitted only from denser regions. Higher-order Lyman photons can convert to the other hydrogen recombination lines in addition to the emission lines that lower-Lyman photons can produce. The plus symbols before the line names indicate that they are additional lines to the ones shown in the outer layer(s).

4.3 Future work

Beyond the aspects discussed so far, there are other aspects that I plan to explore to advance the understanding of dust attenuation curves within simulated galaxies.

Firstly, I plan to make direct comparisons between the derived attenuation curves with unattenuated stellar SEDs, which are accessible with simulated galaxies. The difference between an unattenuated and attenuated SED will directly indicate the underlying attenuation curve. Additionally, this investigation may help reconsideration of the applied shifts to each galaxy (Equation (2.10)).

Secondly, I will explore the impact of galaxy inclinations on attenuation curves. I expect that a galaxy with edge-on view may be more attenuated, as the light has to travel longer pathways, than a face-on view galaxy. The comparison of attenuation curves under different inclinations may contribute to a more comprehensive understanding on how observational perspectives affect the attenuation curves.
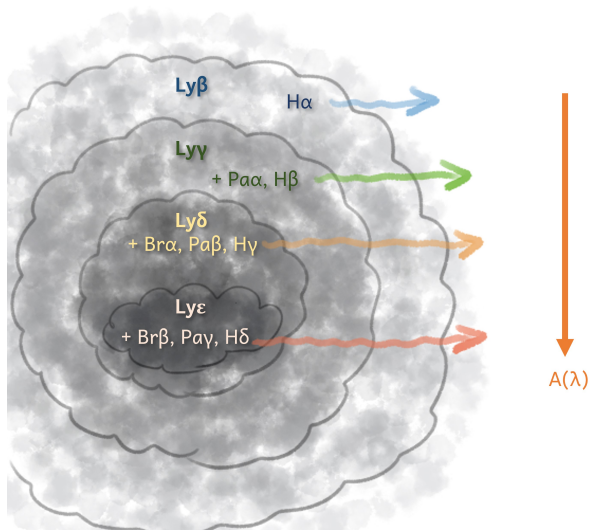
Thirdly, in the current work, I set aside concern on the excess Paβ attenuations and the non-monotonic curves. It will be important to revisit these phenomena to understand dust attenuation curves. The Paβ excess might be attributed to the adopted dust distribution, as the peak of the Mie scatter happens at the wavelength of Paβ. For the non-monotonic curve, its possible cause has already been briefly discussed in Section 4.2. I plan to further explore if these hypotheses are plausible.

Finally, as briefly discussed at the end of Section 4.2, Hγ line fitting needs to be refined. I will include the CaI absorption line (0.4307 μm) simultaneously for the fit to obtain more accurate Hγ line fluxes. I will then revisit $\log(H\gamma/H\delta)$ to compare with the Case B condition.

Chapter 5

Conclusions

In this study, I use a sample of 100 simulated galaxies to derive dust attenuation curves directly from 10 hydrogen recombination lines from Hδ (0.41 μm) to Brα (4.05 μm). The spectral lines were extracted from SEDs constructed by the dust radiation transfer package, POWDERDAY. I employ a quadratic-in-1/lambda function to model a hydrogen line attenuation curve for each galaxy. Various normalizations are applied to express the curves in the form of $A(\lambda)$, $k'(\lambda)$, and $A(\lambda)/A(V)$. I confirm a wide variation of the curves among galaxies, including in the NIR wavelength range. A subset of the galaxies yield non-monotonic (rising) curves in the NIR range, which, although excluded in this current investigation, warrants future exploration. I also investigate relations between the attenuation curves and galaxy properties. There are no obvious relations with various masses, star formation rates, and metallicity. This suggests that other properties that are still not fully incorporated in galaxy formation simulations (e.g., grain size distributions) or local geometries play a more dominant role in shaping nebular dust attenuation curves than global galaxy properties.

# Acknowledgements

Appendix A

The dust attenuation curves

Here I show the fits to attenuation values of hydrogen recombination lines (left column), attenuation curves normalized by $E(B-V)$ (middle column), and attenuation curves normalized by A_V (right column), as derived in this work. Each row shows the results from a single galaxy with its ID number displayed at the bottom left in each panel. Only the galaxies with monotonic attenuation curves are listed. The reduced χ^2 of the fits can be found at the top right in each panel. As discussed in the main text (Section 2.2.3), Paβ, denoted by an empty circle, is not included in the fits.
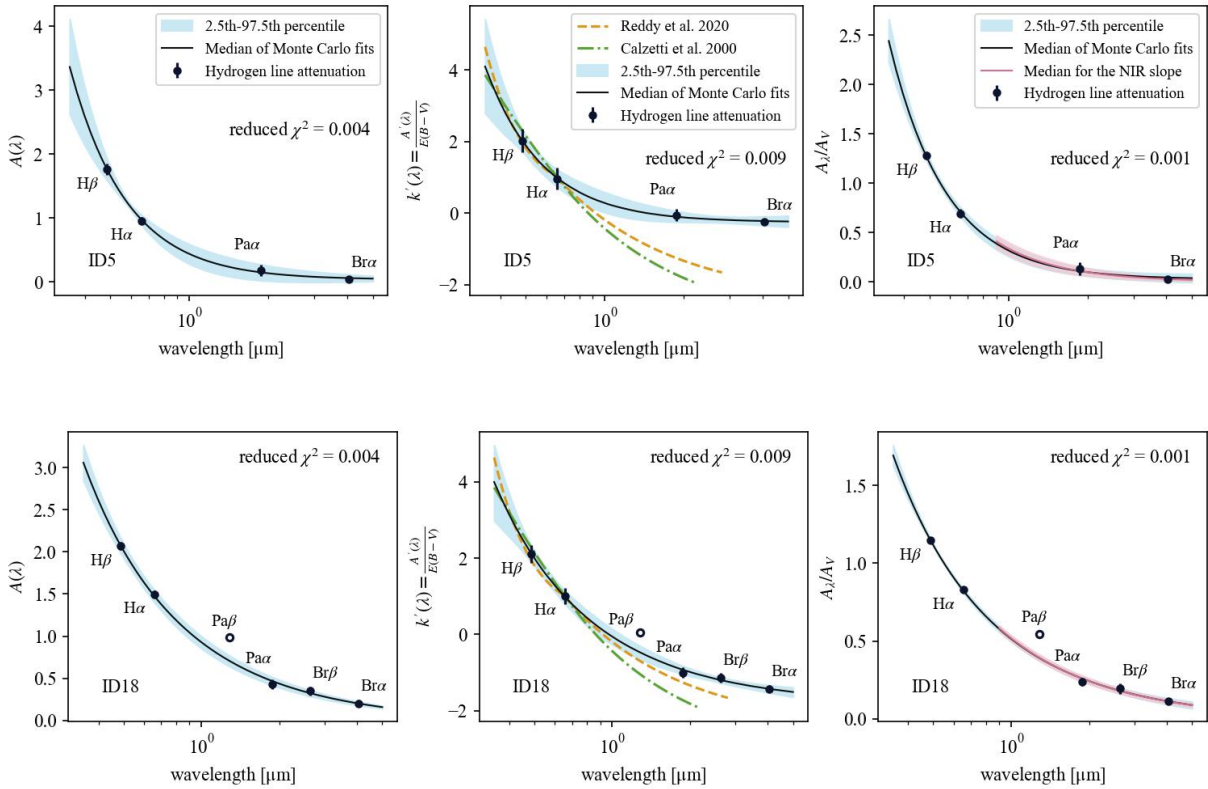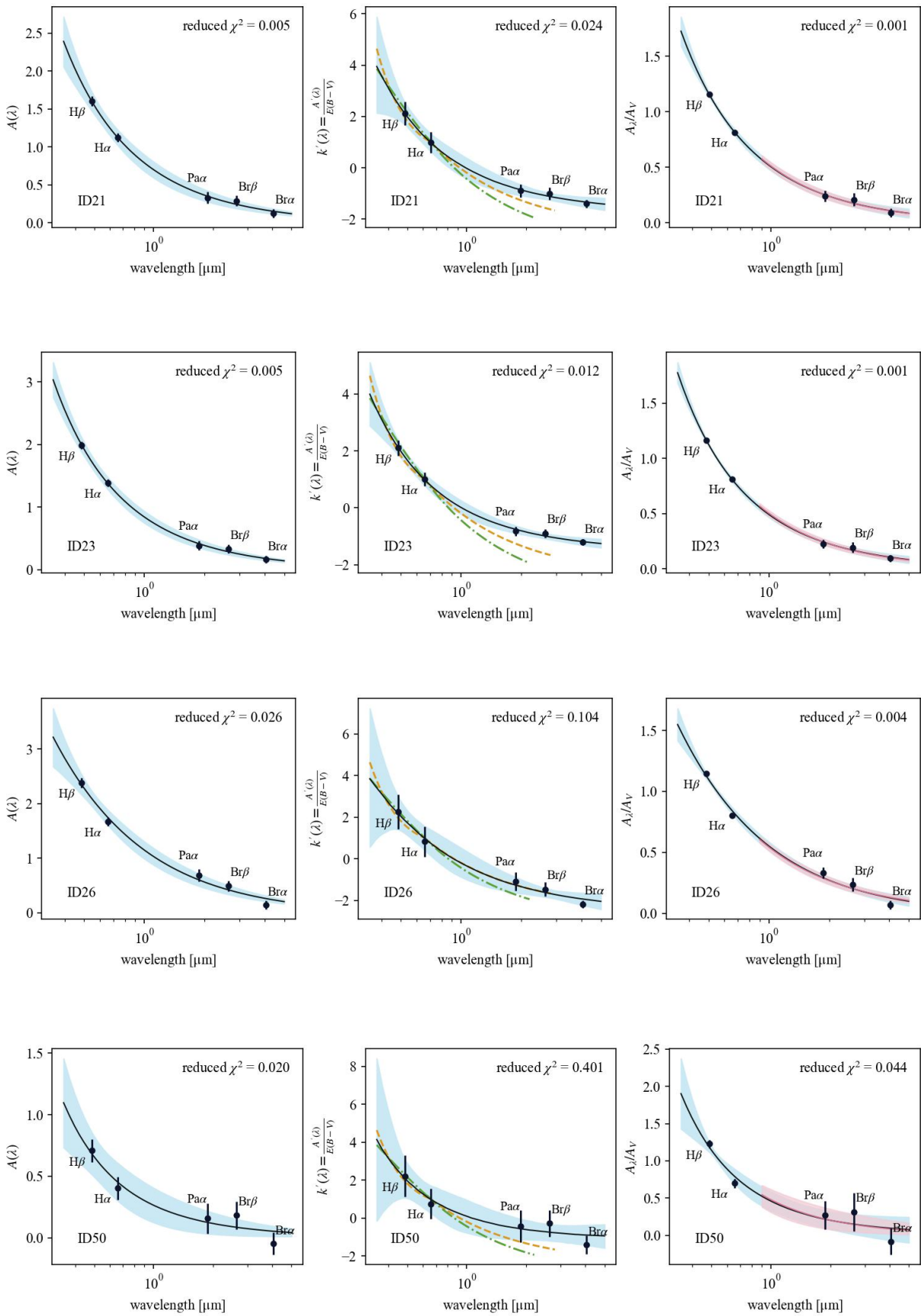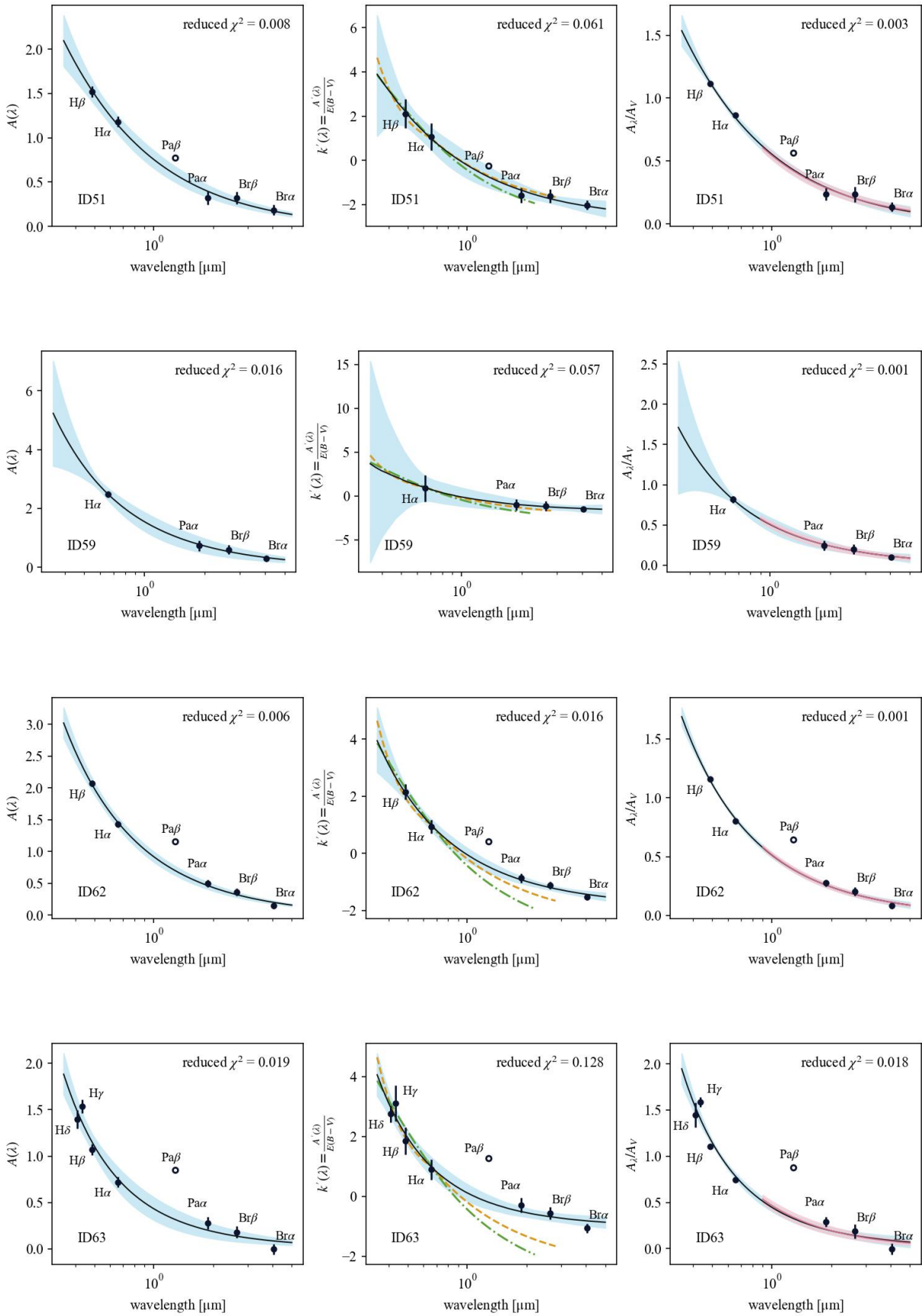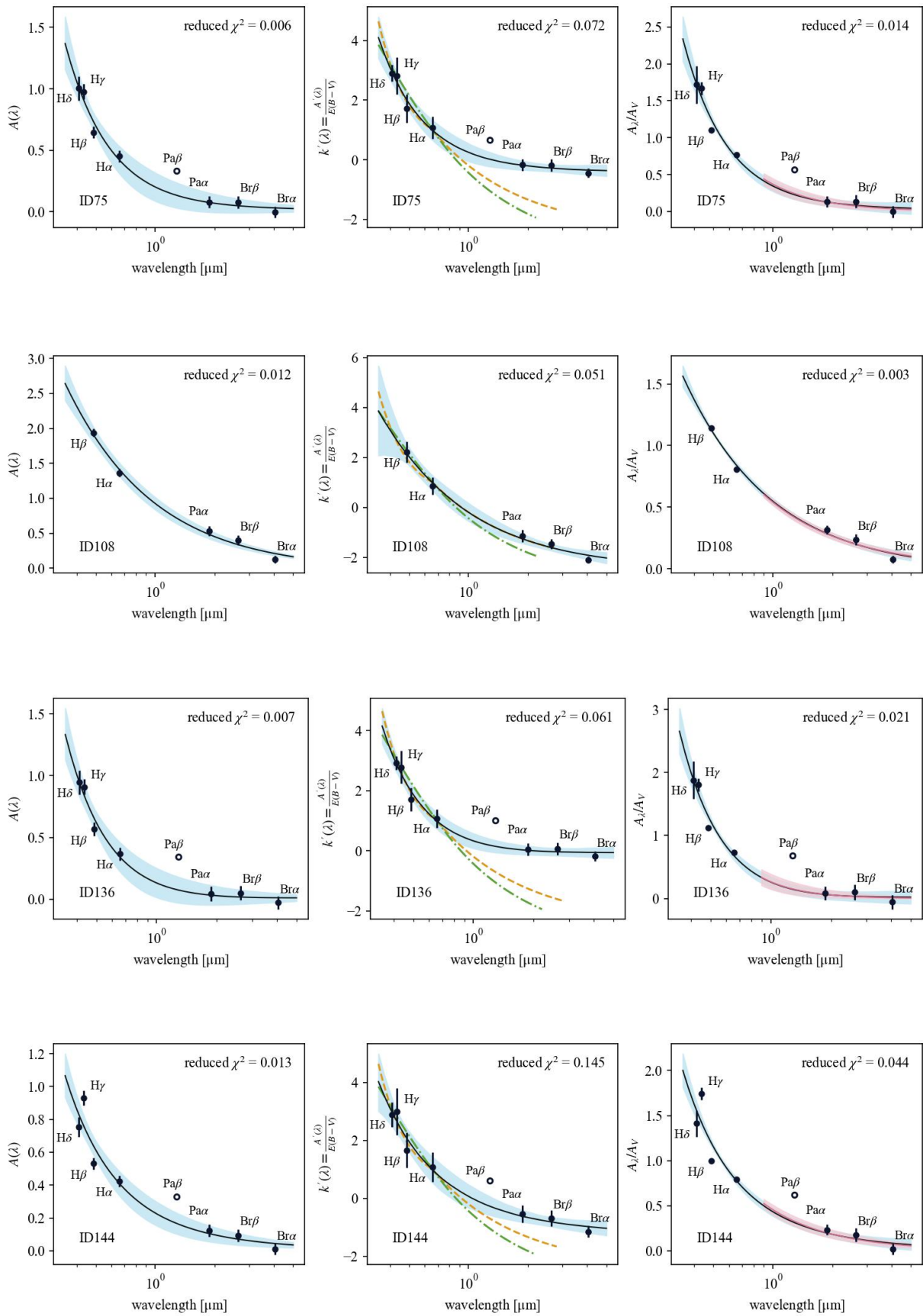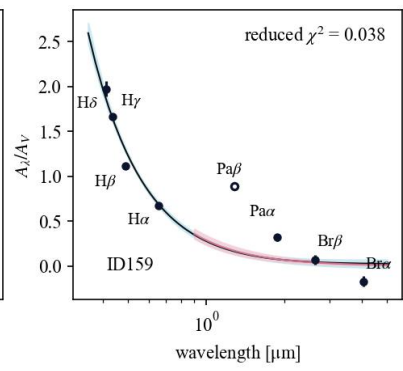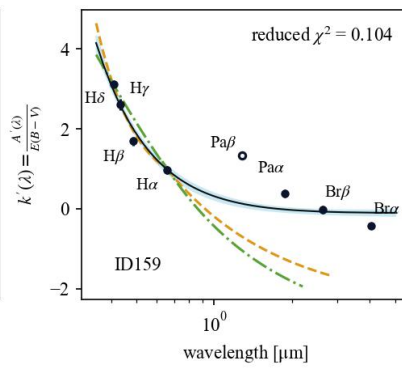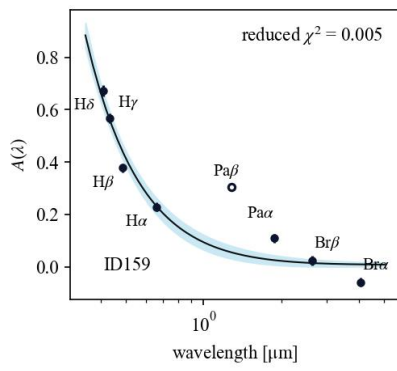
Bibliography

Naveen A. Reddy, Alice E. Shapley, Mariska Kriek, Charles C. Steidel, Irene Shivaei, Ryan L. Sanders, Bahram Mobasher, Alison L. Coil, Brian Siana, William R. Freeman, Mojegan Azadi, Tara Fetherolf, Gene Leung, Sedona H. Price, and Tom Zick. The MOSDEF Survey: The First Direct Measurements of the Nebular Dust Attenuation Curve at High Redshift. *The Astrophysical Journal*, 902(2):123, October 2020. doi: 10.3847/1538-4357/abb674.

Yasuo Fukui, Shuichiro Inutsuka, Toshikazu Onishi, Naomasa Nakai, Toshinori Maihara, and Akira Mizuno. 星間物質と星形成. シリーズ現代の天文学, 6 巻. 日本評論社, 2008. ISBN 9784535607262.

Yoshiaki Taniguchi, Sadanori Okamura, and Yoshiaki Sofue. 銀河と宇宙の階層構造. シリーズ現代の天文学, 4 巻 (第 2 版). 日本評論社, 2018. ISBN 9784535607545.

Ralf S. Klessen and Simon C. O. Glover. Physical Processes in the Interstellar Medium. In Yves Revaz, Pascale Jablonka, Romain Teyssier, and Lucio Mayer, editors, *Saas-Fee Advanced Course*, volume 43 of *Saas-Fee Advanced Course*, page 85, January 2016. doi: 10.1007/978-3-662-47890-5_2.

Masayuki Umemura, Jun Fukue, and Hideko Nomura. 輻射輸送と輻射流体力学. シリーズ〈宇宙物理学の基礎〉, 3 巻. 日本評論社, 2016. ISBN 978-4-535-60342-4.

Hannu Karttunen, Pekka Kröger, Heikki Oja, Markku Poutanen, and Karl Johan Donner. *Fundamental Astronomy*. 5th. Springer Berlin, Heidelberg, 2007. ISBN 978-3-642-42110-5. doi: 10.1007/978-3-540-34144-4.

Mordecai-Mark Mac Low. From Gas to Stars Over Cosmic Time. *Science*, 340(6140):1229229, June 2013. doi: 10.1126/science.1229229.

Samir Salim and Desika Narayanan. The Dust Attenuation Law in Galaxies. *Annual Review of Astronomy and Astrophysics*, 58:529–575, August 2020. doi: 10.1146/annurev-astro-032620-021933.

Irene Shivaei, Naveen Reddy, George Rieke, Alice Shapley, Mariska Kriek, Andrew Battisti, Bahram Mobasher, Ryan Sanders, Tara Fetherolf, Mojegan Azadi, Alison L. Coil, William R. Freeman, Laura de Groot, Gene Leung, Sedona H. Price, Brian Siana, and Tom Zick. The MOSDEF Survey: The Variation of the Dust Attenuation Curve with Metallicity. *The Astrophysical Journal*, 899(2):117, August 2020. doi: 10.3847/1538-4357/aba35e.

Kuan-Chou Hou, Hiroyuki Hirashita, Kentaro Nagamine, Shohei Aoyama, and Ikkoh Shimizu. Evolution of dust extinction curves in galaxy simulation. *Monthly Notices of the Royal Astronomical Society*, 469 (1):870–885, July 2017. doi: 10.1093/mnras/stx877.

B. Lo Faro, V. Buat, Y. Roehlly, J. Alvarez-Marquez, D. Burgarella, L. Silva, and A. Efstathiou. Characterizing the UV-to-NIR shape of the dust attenuation curve of IR luminous galaxies up to z ~ 2. *Monthly Notices of the Royal Astronomical Society*, 472(2):1372–1391, December 2017. doi: 10.1093/mnras/stx1901.

Daniela Calzetti, Lee Armus, Ralph C. Bohlin, Anne L. Kinney, Jan Koornneef, and Thaisa Storchi-Bergmann. The Dust Content and Opacity of Actively Star-forming Galaxies. *The Astrophysical Journal*, 533(2):682–695, April 2000. doi: 10.1086/308692.

Desika Narayanan, Matthew J. Turk, Thomas Robitaille, Ashley J. Kelly, B. Connor McClellan, Ray S. Sharma, Prerak Garg, Matthew Abruzzo, Ena Choi, Charlie Conroy, Benjamin D. Johnson, Benjamin Kimock, Qi Li, Christopher C. Lovell, Sidney Lower, George C. Privon, Jonathan Roberts, Snigdaa Sethuram, Gregory F. Snyder, Robert Thompson, and John H. Wise. POWDERDAY: Dust Radiative Transfer for Galaxy Simulations. *The Astrophysical Journal Supplement Series*, 252(1):12, January 2021. doi: 10.3847/1538-4365/abc487.

Sidney Lower, Desika Narayanan, Joel Leja, Benjamin D. Johnson, Charlie Conroy, and Romeel Davé. How Well Can We Measure Galaxy Dust Attenuation Curves? The Impact of the Assumed Star-dust Geometry Model in Spectral Energy Distribution Fitting. *The Astrophysical Journal*, 931(1):14, May 2022. doi: 10.3847/1538-4357/ac6959.

Donald E. Osterbrock and Gary J. Ferland. *Astrophysics of gaseous nebulae and active galactic nuclei*. 2006.

G. H. Rieke and M. J. Lebofsky. The interstellar extinction law from 1 to 13 microns. *The Astrophysical Journal*, 288:618–621, January 1985. doi: 10.1086/162827.